

Porphyrinic metal-organic frameworks as molybdenum adsorbents for the $^{99}\text{Mo}/^{99\text{m}}\text{Tc}$ generator

Ma, Chao; Wolterbeek, Hubert T.; Denkova, Antonia G.; Serra Crespo, Pablo

DOI

[10.1039/d2qi01919a](https://doi.org/10.1039/d2qi01919a)

Publication date

2023

Document Version

Final published version

Published in

Inorganic Chemistry Frontiers

Citation (APA)

Ma, C., Wolterbeek, H. T., Denkova, A. G., & Serra Crespo, P. (2023). Porphyrinic metal-organic frameworks as molybdenum adsorbents for the $^{99}\text{Mo}/^{99\text{m}}\text{Tc}$ generator. *Inorganic Chemistry Frontiers*, 10(8), 2239-2249. <https://doi.org/10.1039/d2qi01919a>

Important note

To cite this publication, please use the final published version (if applicable).
Please check the document version above.

Copyright

Other than for strictly personal use, it is not permitted to download, forward or distribute the text or part of it, without the consent of the author(s) and/or copyright holder(s), unless the work is under an open content license such as Creative Commons.

Takedown policy

Please contact us and provide details if you believe this document breaches copyrights.
We will remove access to the work immediately and investigate your claim.

RESEARCH ARTICLE

View Article Online
View Journal

Cite this: DOI: 10.1039/d2qi01919a

Porphyrinic metal–organic frameworks as molybdenum adsorbents for the $^{99}\text{Mo}/^{99\text{m}}\text{Tc}$ generator†

Chao Ma, , Hubert T. Wolterbeek, Antonia G. Denkova* and Pablo Serra Crespo *

Two porphyrinic metal–organic frameworks (PCN-222 and PCN-224) were prepared and their potential as molybdenum adsorbents for the $^{99}\text{Mo}/^{99\text{m}}\text{Tc}$ generator was explored. The molybdenum adsorption properties of the two adsorbents, including adsorption kinetics and equilibrium isotherms, were evaluated at different molybdenum concentrations and pH. The maximum adsorption capacity of PCN-222 and PCN-224 was evaluated to be 525 mg g^{-1} and 455 mg g^{-1} , respectively. The possible adsorption mechanism was investigated by X-ray Photoelectron Spectra and Fourier-Transform Infrared Spectroscopy. The results demonstrated that molybdenum species were adsorbed on the two MOFs through electrostatic attraction and hydrogen bonds. In the case of PCN-222, the Mo–O–Zr coordination interaction also played an important role. Additionally, the elution performance of two $^{99}\text{Mo}/^{99\text{m}}\text{Tc}$ generators developed by using PCN-222 and PCN-224 as adsorbents was measured to assess possible clinical applications. The PCN-222-based $^{99}\text{Mo}/^{99\text{m}}\text{Tc}$ generator exhibited better elution performance and showed that around 56% of $^{99\text{m}}\text{Tc}$ could be obtained without zirconium breakthrough when relatively high pH solutions were used (pH = 9.6).

Received 5th September 2022,
Accepted 30th November 2022

DOI: 10.1039/d2qi01919a

rsc.li/frontiers-inorganic

1. Introduction

Technetium-99 m ($^{99\text{m}}\text{Tc}$) is the most utilized radionuclide in nuclear medicine, being applied in more than 30 million diagnostic procedures annually all over the world.^{1,2} This huge demand is attributed to its low gamma energy emission and short half-life (6 h), which allow for diagnosis without exposing patients to high radiation dose. The rich chemistry of technetium further facilitates the preparation of various diagnostic radiopharmaceuticals. In addition, $^{99\text{m}}\text{Tc}$ can be produced by the β^- decay of Molybdenum-99 (^{99}Mo) from the $^{99}\text{Mo}/^{99\text{m}}\text{Tc}$ generator, which provides a convenient and reliable supply of this radionuclide in nuclear medicine departments all over the world.³

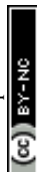
Currently, most of the ^{99}Mo is produced by the fission of enriched uranium-235 in six nuclear reactors worldwide.⁴ Unfortunately, the reliability of ^{99}Mo production has been affected in the past few years due to sudden shutdowns and

maintenance of some reactors, leading to a global ^{99}Mo supply shortage in 2009.⁵ In addition, this route has a ^{99}Mo yield of 6.1%, producing a huge amount of nuclear waste.^{6,7} Due to these main problems, alternative production routes to produce ^{99}Mo have been explored, such as the (n, γ) and (γ , n) reactions from ^{98}Mo and ^{100}Mo respectively. If those routes became a reality, more than 75 research reactors and many accelerators worldwide could be utilized to produce ^{99}Mo .^{8,9}

However, ^{99}Mo produced by (n, γ) and (γ , n) reactions has low specific activity and the commercial generator material cannot be used because of the low adsorption capacity of the alumina column ($2\text{--}20\text{ mg g}^{-1}$) currently used.¹⁰ There are two options to overcome this limitation. One of the solutions is increasing the amount of adsorbents and the other one is exploring new adsorbents with higher adsorption capacity. Using more adsorbents is not a desired option, since it will increase the size of the generator causing more shielding and costs. Furthermore, large elution volumes will produce $^{99\text{m}}\text{Tc}$ with low concentration, which complicates its medical application. Therefore, it is necessary to develop adsorbents with a higher adsorption capacity. Many efforts have been carried out to implement the use of low specific activity ^{99}Mo by investigating porous materials with good adsorption properties. Some traditional materials such as mesoporous Al_2O_3 ,¹¹ Al-TUD-1,¹² TiO_2 ,¹³ ZrO_2 and CeO_2 ^{14–16} were researched as adsor-

Applied radiation and isotopes, Radiation Science and Technology, Faculty of Applied Sciences, Delft University of Technology, 2629 JB Delft Mekelweg 15, The Netherlands.
E-mail: A.G.Denkova@tudelft.nl, P.SerraCrespo@tudelft.nl

† Electronic supplementary information (ESI) available. See DOI: <https://doi.org/10.1039/d2qi01919a>



bents to develop a $^{99}\text{Mo}/^{99\text{m}}\text{Tc}$ generator. In all cases, improved molybdenum adsorption capacities ($50\text{--}230\text{ mg g}^{-1}$) with acceptable $^{99\text{m}}\text{Tc}$ elution efficiency have been achieved. However, these new adsorbents still have limited surface area and adsorption sites, which restricts fabricating clinical-grade $^{99}\text{Mo}/^{99\text{m}}\text{Tc}$ generator for widespread application in nuclear medicine. Hence, the development of new-generation adsorbents with higher adsorption capacity is very meaningful and necessary to realize a generator available for clinical application using low specific activity ^{99}Mo .

Metal–organic frameworks (MOFs) have gained considerable attention and exhibit excellent prospects in many applications, including purification,^{17,18} drug delivery,¹⁹ adsorption and separation^{20,21} because of their high surface area, easily functionalized cavities and controlled porosity.^{22,23} Our previous work showed that UiO-66 MOF was a great adsorbent for the preparation of $^{99}\text{Mo}/^{99\text{m}}\text{Tc}$ generator.^{24,25} Based on the previous promising results we attempted to further increase the adsorption capacity using MOFs. We choose two zirconium

MOFs (PCN-222 and PCN-224) due to their higher surface area and bigger pore sizes, which are expected to result in the high loading of molybdenum ions while retaining their high chemical stability.

Although the structures of PCN-222 and PCN-224 are based on tetra(4-carboxyphenyl) porphyrin (TCPP) linker, they have 8 and 6 linker coordination with Zr₆ clusters, respectively. PCN-222 has two types of pores, *i.e.* micropores with a diameter of $\sim 1.2\text{ nm}$ and mesopores with a diameter of $\sim 3.7\text{ nm}$, while PCN-224 has only micropores with a diameter of $\sim 1.9\text{ nm}$ (as shown in Fig. 1). In this work, we synthesized the two MOFs and evaluated their Mo adsorption performance including kinetics, isotherms and capacity at different Mo concentrations and pH. Furthermore, the adsorption mechanism was also investigated by XPS and FT-IR to reveal the interaction between Mo species and the adsorbents. Finally, adsorption batch and column experiments using ^{99}Mo were carried out to determine their potential as adsorbents for $^{99}\text{Mo}/^{99\text{m}}\text{Tc}$ generator.

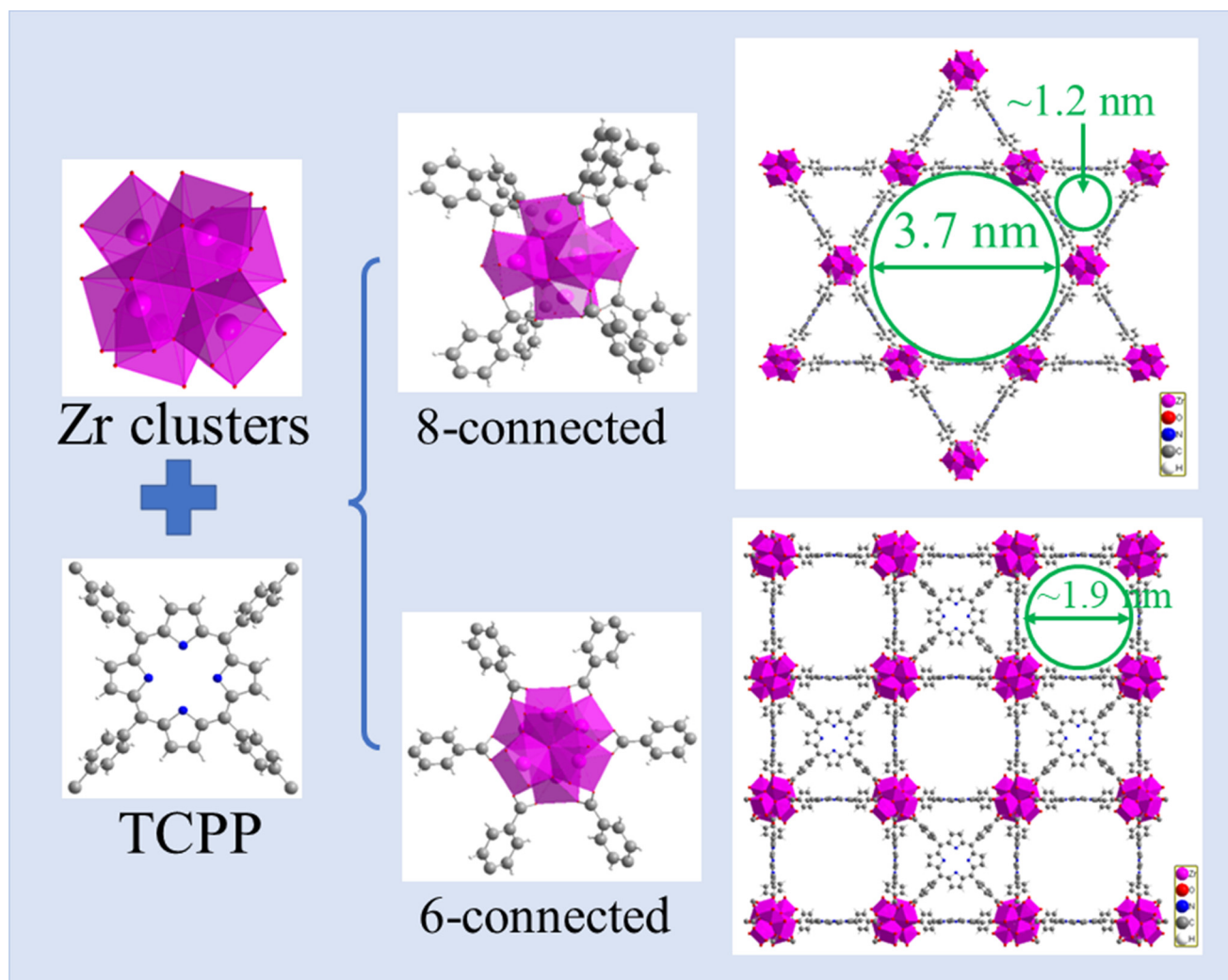


Fig. 1 The crystallographic structures of PCN-222 and PCN-224. Color: C, gray; O, red; H, white; N, blue; Zr, pink.



2. Experimental section

2.1 Materials

All chemical reagents were ordered from the indicated suppliers and used without further purification. Zirconium(IV) chloride ($\geq 99.5\%$) was purchased from Alfa Aesar. *N,N*-Dimethylformamide (DMF, 99.8%), benzoic acid ($\geq 99.5\%$), Tetrakis(4-carboxyphenyl) porphyrin (97%) were purchased from Sigma Aldrich.

2.2 Synthesis of PCN-222 and PCN-224

PCN-222 was synthesized based on previous literature with a few modifications using the solvothermal method.^{26,27} First, 150 mg of $\text{ZrOCl}_2 \cdot 8\text{H}_2\text{O}$ (465 μmol) was added to 40 mL of DMF by magnetic stirring for 30 min and 116 mg of TCPP (147 μmol) was added afterward. Then, 19 mL of formic acid solution was introduced and the mixture was further stirred for 15 min. Finally, the solution was transferred to a Teflon-lined autoclave and heated at 130 °C for 3 days. After cooling down to room temperature, the precipitation was collected and washed with DMF and acetone for three times, respectively. The final product was dried at room temperature.

The synthesis of PCN-224 was prepared according to previous research.²⁸ Briefly, 30 mg of ZrCl_4 , 10 mg of TCPP and 400 mg of benzoic acid were ultrasonically dissolved for 20 min in 2 mL of DMF. Then the solution was heated at 120 °C for 24 h by an electric furnace. After cooling to room temperature, the precipitation was washed with DMF and acetone three times, respectively. Finally, the sample was immersed in acetone for over 12 h and dried at 80 °C for 6 h under vacuum.

2.3 Characterization

Powder X-ray diffraction was collected with PANalytical X'Pert Pro pw3040/60 diffractometer equipped with Cu K α radiation under the condition of 45 kV and 40 mA. Nitrogen adsorption at 77 K was performed using a Micromeritics Tristar II and the samples were pre-treated at 150 °C for 16 h under vacuum before measurement. Fourier-transform infrared spectroscopy (FT-IR) was carried out by a NICOLET 6700 instrument in a wavenumber range of 400–4000 cm^{-1} at room temperature. The crystal morphology was observed using scanning electron microscopy (Leo Supra 50, Zeiss). The zeta potential was collected in a pH range of 2–10 to determine the surface charge of adsorbents by a Malvern ZetaSizer nano-ZS instrument. The suspension was prepared by dispersing 0.3 ± 0.1 mg of sample into 1 mL of solutions with different pH values. The concentration of the different molybdenum solutions was determined by inductively coupled plasma optical emission spectroscopy (ICP-OES, Optima 4300, Perkin and Elmer). The chemical states of composing elements of MOFs were analyzed by K-Alpha X-ray photoelectron spectra (XPS, ThermoFisher Scientific).

2.4 Molybdenum adsorption

Molybdenum adsorption isotherms of PCN-222 and PCN-224 were carried out at different pH (2–9) and initial molybdenum concentrations (0.1–20 mg mL^{-1}) by batch experiments. The stock solution was prepared by dissolving 3 g of MoO_3 into 1.8 g of NaOH (1M) solution and the pH of the solution was adjusted to predetermined values. Then, the stock solution was diluted to prepare molybdenum solutions with different concentrations. Typically, 6 ± 0.5 mg of adsorbent was added into Eppendorf tubes containing 1 mL Mo solution with different initial concentrations. The mixture was shaken at 25 °C for 24 h by a temperature-controlled shaker with 1400 rpm. Then all Eppendorf tubes were centrifuged and the concentration in the supernatant was analyzed by ICP-OES. The molybdenum uptake of the adsorbents in batch was determined by the following equation:

$$q_e = \frac{(C_0 - C_e) \times V}{m} \quad (1)$$

where q_e and C_e (mg mL^{-1}) are the molybdenum uptake and concentration at equilibrium, respectively. C_0 represents the initial Mo concentration. V (mL) denotes the volume of solution and m (mg) is the mass of the adsorbent. The molybdenum adsorption kinetics and the effect of pH on adsorption were also carried out and more details can be found in the ESI.†

3. Results and discussion

3.1 Molybdenum adsorption studies

3.1.1 Effects of pH. The effects of pH on the Mo adsorption on PCN-222 and PCN-224 were conducted in a pH range of 2–10 and initial molybdenum concentration of 5 mg mL^{-1} . The results are shown in Fig. 2(a). It can be observed that the molybdenum uptake of PCN-222 decreased continuously from 457 mg g^{-1} (pH = 2) to 140 mg g^{-1} (pH = 10) with increasing pH value. The uptake on PCN-224 decreased slightly from pH 2 (332 mg g^{-1}) to 3 (321 mg g^{-1}) and then decreased to 145 mg g^{-1} at pH 8.7. The zeta potential, which reflects the surface charge of the adsorbents, is shown in Fig. 2(b). The isoelectric points (IEPs) of PCN-222 and PCN-224 are between 6.5 and 7. Meanwhile, the molybdenum species present in the solution vary with the molybdenum concentration and the pH of the solution. According to previously reported literature,^{29,30} when molybdenum solution of 0.01 M is used, the major molybdenum chemical species is $\text{Mo}_7\text{O}_{24}^{6-}$ at a pH range between 2 and 5; at pH > 5 the dominant species is MoO_4^{2-} (see in Fig. S1†). When the pH value is less than IEPs, the adsorbents have positive charges that can interact with the negatively charged molybdenum species by electrostatic attraction. However, when the pH value is higher than IEPs, the adsorption of two adsorbents was found to be still around 140 mg g^{-1} , which suggests that chemisorption plays a role.

3.1.2 Adsorption kinetics. The molybdenum adsorption kinetics of PCN-222 and PCN-224 were measured with starting



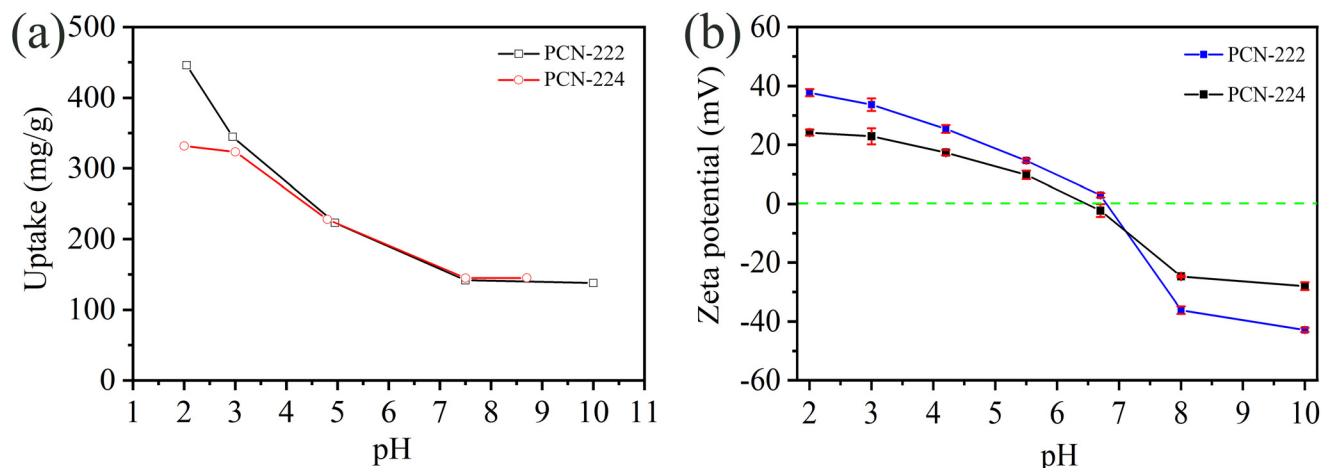


Fig. 2 (a) Effect of pH on the Mo adsorption on PCN-222 and PCN-224 when the initial Mo concentration was 5 mg mL^{-1} ; (b) zeta potential of PCN-222 and PCN-224 as function of pH.

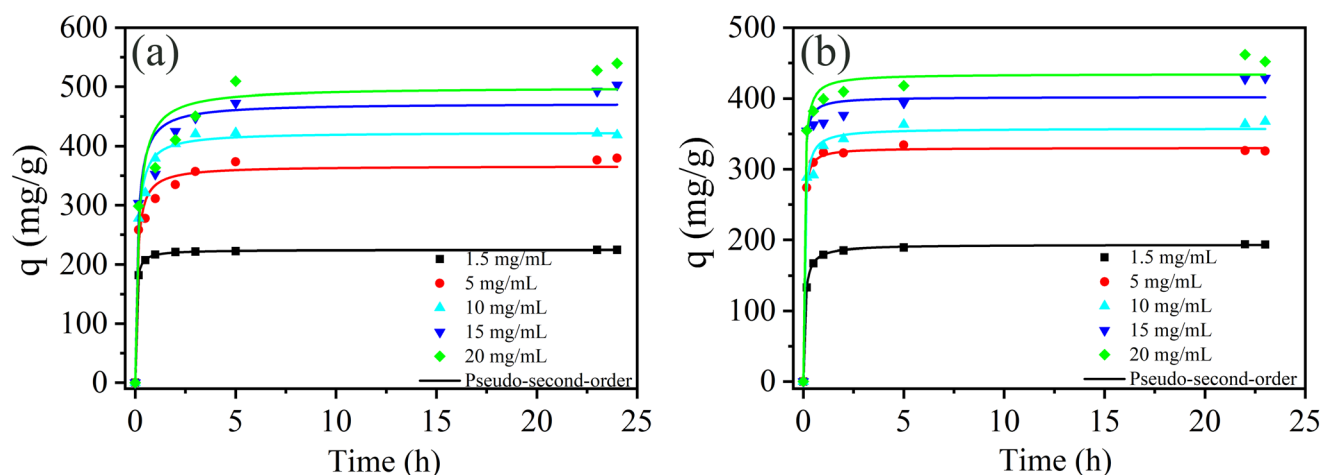


Fig. 3 Molybdenum adsorption kinetics of (a) PCN-222 and (b) PCN-224 at different molybdenum concentration (pH = 3).

concentrations from 1.5 mg mL^{-1} to 20 mg mL^{-1} and the results are shown in Fig. 3(a) and (b). The molybdenum adsorption uptake of PCN-222 reached equilibrium after 1 h with an uptake of $\sim 220 \text{ mg g}^{-1}$ when the initial molybdenum concentration was 1.5 mg mL^{-1} . The adsorption processes reached equilibrium within 3 h when the initial molybdenum concentrations were 5 mg mL^{-1} and 10 mg mL^{-1} . With increasing molybdenum concentration (15 mg mL^{-1} and 20 mg mL^{-1}), the adsorption approached equilibrium after 5 h. This adsorption phenomenon could be attributed to the dimensions of the molybdenum species and the pore size of the adsorbent. At the initial adsorption stage, the molybdenum species would occupy the preferential adsorption sites of PCN-222. Subsequently, the large concentration gradient promotes the diffusion of molybdenum ions to the remaining adsorption sites. When the molybdenum concentration is 1 mM ($\text{ca. } 0.1 \text{ mg mL}^{-1}$) at pH = 3, MoO_4^{2-} is the dominant molybdenum species. When molybdenum concentration is 0.1

M ($\text{ca. } 10 \text{ mg mL}^{-1}$) at pH = 3, the main molybdenum species is $\text{Mo}_8\text{O}_{26}^{4-}$. Molybdenum species with small sizes at low concentrations could rapidly diffuse into the micropores ($\sim 1.2 \text{ nm}$) and mesopores ($\sim 3.7 \text{ nm}$) in PCN-222. At higher concentrations, molybdenum species with larger sizes would have a relatively slow diffusion rate, taking longer to access the porous structure. In comparison, the adsorption uptake of PCN-224 can reach 90% of the total adsorption capacity within 1 hour and equilibrium within 2 hours, which appears not to be influenced much by the molybdenum concentration due to the larger pore size combined with the smaller crystal size of PCN-224. In addition, Liu *et al.* reported that the particle size of the adsorbent has been shown to have a significant effect on the adsorption kinetics.³¹ The morphology and size of two PCN MOFs were characterized, as shown in Fig. S3.† PCN-222 showed the morphology of hexagonal rod-like crystals and smooth surface, displaying a width of $2\text{--}4 \mu\text{m}$ and lengths of dispersed $10\text{--}50 \mu\text{m}$ dimensions, most likely due to breakage



of the crystals. PCN-224 exhibited round rod structure with a diameter of around 200–400 nm and length from 1 to 10 μm . Therefore, the bigger particle size and small windows on the microporous of PCN-222 limit the diffusion of molybdenum species, leading to slower adsorption and residual surface area after adsorption (Fig. 5(c)). To further analyze the adsorption process, the pseudo-first-order and pseudo-second-order models were employed to fit the experimental data (see ESI†). The calculated parameters are summarised in Tables S1 and S2.† The pseudo-second kinetic model of PCN-222 and PCN-224 has higher correlation coefficient values ($R^2 > 0.999$) than the pseudo-first-order model, indicating that the Mo adsorption process can be better described by the pseudo-second kinetic model. Furthermore, the calculated adsorption capacities by the pseudo-second kinetic model are consistent with experimental data for two MOFs, which also indicates the existence of a chemisorption process.

3.1.3 Molybdenum adsorption isotherms. Molybdenum adsorption isotherms of PCN-222 and PCN-224 were measured at pH 3 as function of the equilibrium molybdenum concentration to determine the molybdenum adsorption capacity, and the results are displayed in Fig. 4(a) and (b). Their molybdenum uptake increased to around 350 mg g^{-1} and can exceed 70% of the adsorption saturation value at low molybdenum concentration ($C_{\text{Mo}} < 5 \text{ mg mL}^{-1}$). The maximum molybdenum adsorption capacity of PCN-222 was determined to be around 525 mg g^{-1} , which is higher than that of PCN-224 (455 mg g^{-1}). To better estimate the adsorption behaviour, the Freundlich and Langmuir models were applied to fit the obtained data. The fitted results are depicted in Table S3.† The R^2 values suggested that the Freundlich model could better fit the molybdenum adsorption isotherms of PCN-222 (96.1%) and PCN-224 (99.7%), which indicated that the adsorption was multilayer adsorption on heterogeneous surface.³² The molybdenum adsorption capacity of PCN-222 is larger than that of PCN-224, which may be attributed to its higher surface area and larger pore size than PCN-224. Moreover, both adsorbents exhibit excellent Mo adsorption performance compared to the

Table 1 Summary of the static Mo adsorption capacity of various adsorbents

Adsorbents	Mo adsorption capacity (mg g^{-1})	Surface area ($\text{m}^2 \text{g}^{-1}$)	Ref.
TUD-1	112	402	12
Hydrous MnO_2	50	—	33
Hydrous TiO_2	230	—	13
Al-dropped mesoporous SiO_2	16.8	463	34
Mesoporous $\gamma\text{-Al}_2\text{O}_3$	56.2	251	35
Nanocrystalline $\gamma\text{-Al}_2\text{O}_3$	200	252	36
Nano $\text{Zr}(\text{OH})_4$ gel	292	151	37
Macro/mesoporous $\gamma\text{-Al}_2\text{O}_3$	250	542	38
Al^{99}Mo gel	364	—	39
UiO-66 (Zr)	335	1624	24
Form-UiO-66	296	1653	24
UiO-66- NH_2	131	295	24
UiO-66- NO_2	227	575	24
UiO-66 (Ce)	475	1140	25
PCN-222	525	1882	This work
PCN-224	455	1467	This work

previously reported adsorbents (Table 1). When compared to other MOFs, UiO-66 (Zr) has a relatively lower adsorption capacity (335 mg g^{-1}) because of its smaller pore size, which restricts the adsorption of large-sized molybdenum species.²⁴ UiO-66 (Ce) has adsorption capacity of 475 mg g^{-1} due to the formed defects that generated extra adsorption sites.²⁵

3.2 Molybdenum adsorption mechanism

To observe the structural information after molybdenum adsorption, the XRD patterns of PCN-222 and PCN-224 were recorded and are shown in Fig. 5(a) and (b). All diffraction peaks of PCN-222 and PCN-224 before adsorption match well with their corresponding calculated patterns,^{40,41} which demonstrates that PCN-222 and PCN-224 with good crystalline structure were synthesized. After molybdenum adsorption, the intensity of the diffraction pattern of PCN-222 was greatly decreased and the two peaks at 7.09° and 7.29° disappeared,

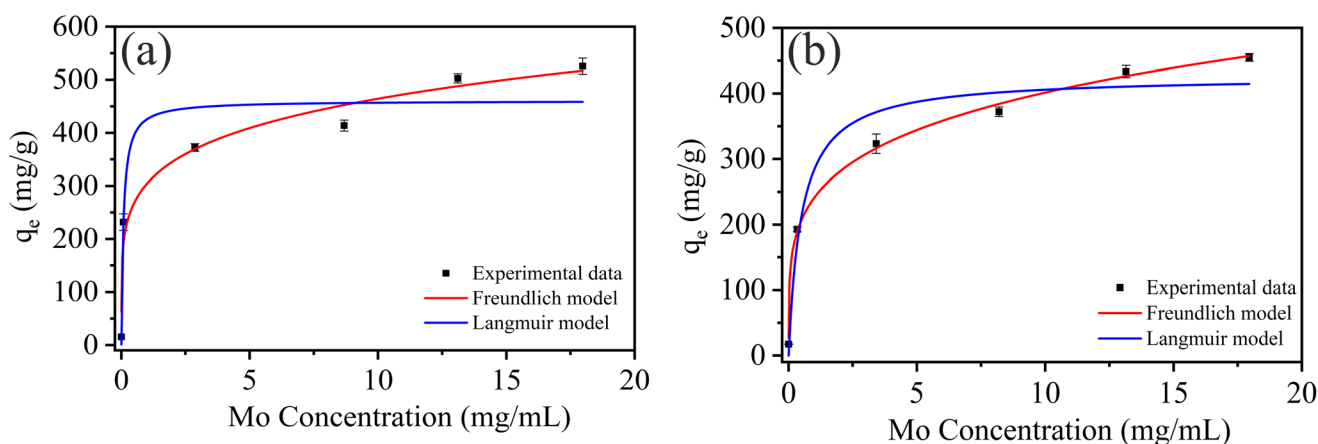


Fig. 4 Molybdenum adsorption isotherm of (a) PCN-222 and (b) PCN-224 at pH 3. Adsorption curves were fitted by the Langmuir (blue) and Freundlich models (red).



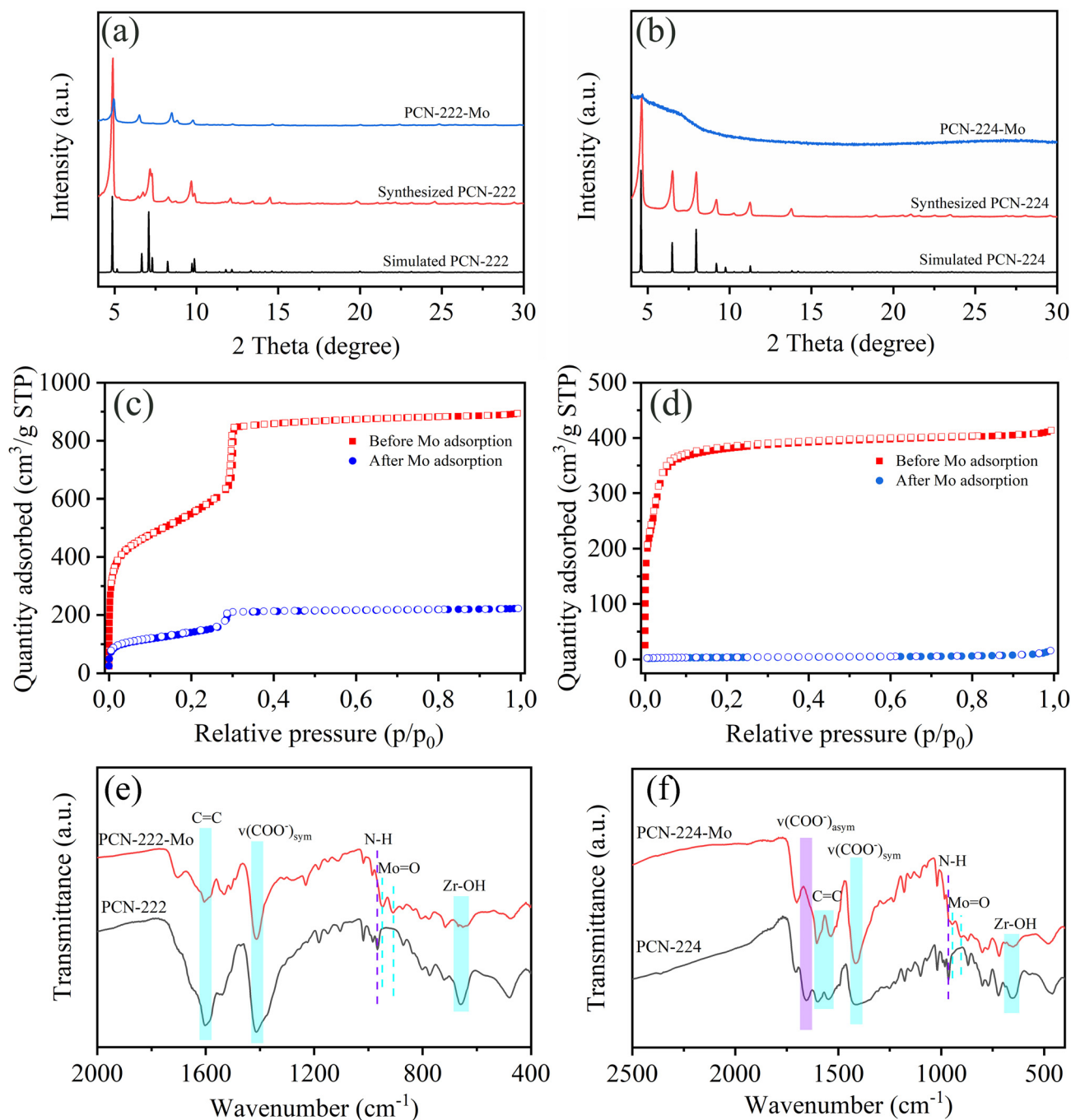


Fig. 5 XRD patterns of (a) PCN-222 and (b) PCN-224; N₂ adsorption isotherms of (c) PCN-222 and (d) PCN-224; FT-IR spectra of (e) PCN-222 and (f) PCN-224 before and after molybdenum adsorption using molybdenum concentration of 20 mg ml⁻¹ (pH = 3).

which can be attributed to the partial occupation of the pores by Mo ions,⁴² causing diminishment of X-ray diffraction. At the same time, all diffraction peaks of PCN-224 disappeared after adsorption except a tiny peak at 4.6° because the material was completely saturated with adsorbed Mo, resulting in a loss of long-range order in the crystal structure of the framework.

The surface area of PCN-222 and PCN-224 was determined by the nitrogen adsorption-desorption technique, as displayed

in Fig. 5(c) and (d). The adsorption isotherms of PCN-222 with a type IV curve have two plateaus at relatively lower pressure and $P/P_0 = 0.3$, corresponding to 1.2 nm micropores and 3.7 nm mesopores, respectively. While the nitrogen adsorption isotherms of PCN-224 belong to the type I curve, indicating microporosity. After molybdenum adsorption, the surface area and pore volume of PCN-222 decreased from 1882 m² g⁻¹ and 1.22 cm³ g⁻¹ to 471 m² g⁻¹ and 0.31 cm³ g⁻¹, respectively (Table S4†), which demonstrates that the molybdenum species



enter the pores of PCN-222, indicating favourable molybdenum adsorption.

The relatively high residual surface area indicates that the material is not fully saturated or that there are some pores that Mo species cannot reach. The surface area and pore volume of PCN-224 before adsorption are $1467 \text{ m}^2 \text{ g}^{-1}$ and $0.56 \text{ cm}^3 \text{ g}^{-1}$, respectively, which decreased to $13 \text{ m}^2 \text{ g}^{-1}$ and $0.002 \text{ cm}^3 \text{ g}^{-1}$ after adsorption, respectively. These results suggest that all the adsorption sites of PCN-224 are accessible and were occupied by molybdenum species.

The FT-IR spectra of PCN-222 and PCN-224 before and after molybdenum adsorption are shown in Fig. 5(e) and (f), respectively. Two new peaks at 908 cm^{-1} and 948 cm^{-1} for both MOFs after adsorption can be observed, demonstrating the presence of the Mo species ($\text{Mo}=\text{O}$).^{43,44} The peak at 650 cm^{-1} , which is attributed to the vibration of $\text{Zr}-\text{OH}$, is weakened for the two materials after adsorption, indicating that there is an interaction between the Mo species and the hydroxyl groups *via* hydrogen bonds.²⁴ The peak at 966 cm^{-1}

corresponding to the N-H in-plane bending vibration of pyrrolic nitrogen disappeared after Mo adsorption,⁴⁵ suggesting an interaction between the $-\text{NH}$ groups and the Mo species.⁴⁶

To explore the possible adsorption mechanism, the surface composition and chemical states of the adsorbents were analyzed by XPS. Fig. 6(a) shows the full view of the XPS spectra of PCN-222 before and after molybdenum adsorption. The primary peaks of C 1s, O 1s, N 1s and Zr 3d can be observed in PCN-222 before and after Mo adsorption. The appearance of new peaks after Mo adsorption at 231.7 eV, 234.87 eV and 415.1 eV, which are attributed to Mo 3d_{5/2}, Mo 3d_{3/2} and Mo 3p, respectively (Fig. 6b), indicates that Mo is successfully adsorbed by the adsorbents. Fig. 6(c) shows the Zr 3d spectra of PCN-222, which was deconvoluted to two peaks of Zr 3d_{5/2} at 182.21 eV and Zr 3d_{3/2} at 184.58 eV.⁴⁷ After Mo adsorption, these two peaks shifted to 181.8 eV and 184.17 eV. The binding energy shifts to lower energy caused by the increased electron density on the Zr surface, which may be ascribed to the formation of Mo-O-Zr coordination bonds *via* donating

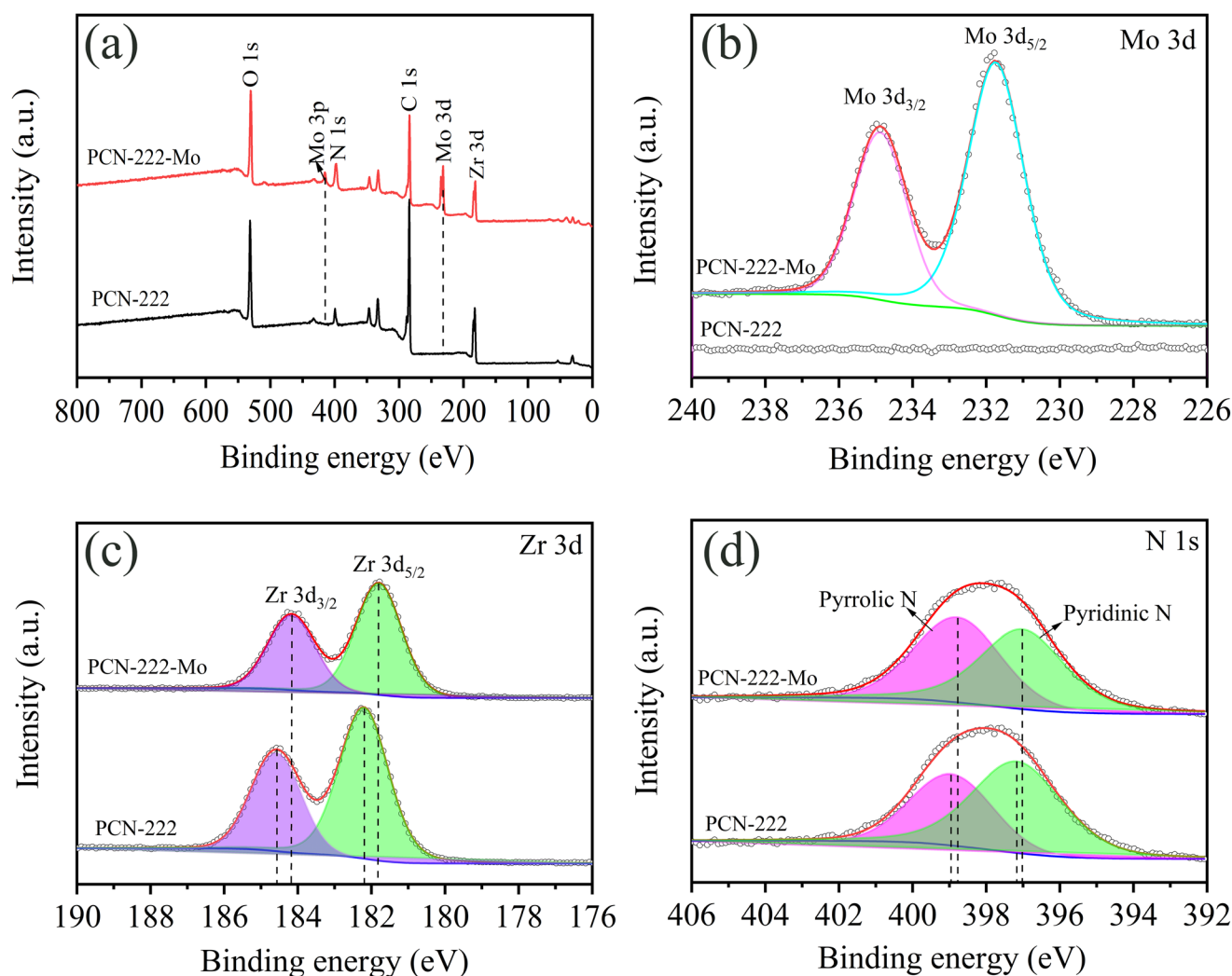


Fig. 6 (a) Full view XPS spectrum; (b) Mo 3d; (c) Zr 3d and (d) N 1s of PCN-222 before and after molybdenum adsorption.



one pair of electrons from the Mo species.²⁴ The N 1s spectrum of PCN-222 before adsorption, as shown in Fig. 6(d), can be divided into two peaks at 398.95 eV and 397.16 eV, which are assigned to pyrrolic N and pyridinic N, respectively.⁴⁸ Their binding energies moved to 398.79 eV and 397.02 eV after Mo adsorption. This small energy shift indicates the weak interaction between Mo species and N atoms. Due to the relatively larger electronegativity of Mo oxyanions, the electron cloud density of N would decrease, leading to the decrease binding energy. Moreover, the C 1s spectra of PCN-222 (Fig. S4†) before adsorption could be divided into three peaks at 284.4 eV, 285.4 eV and 288.2 eV, which are attributed to O=C=O, C=N and C-C/C-H, respectively.⁴⁹

The XPS survey spectra of PCN-224 before and after Mo adsorption is displayed in Fig. 7(a) and the strong peaks of Mo observed for the PCN-224 after adsorption can be observed. High-resolution XPS spectra of Mo 3d is shown in Fig. 7(b) and two peaks at 234.78 eV and 231.61 eV are ascribed to Mo 3d_{3/2} and Mo 3d_{5/2}, respectively. Fig. 7(c) shows the comparison between PCN-224 and PCN-224-Mo and no shifts can be observed, indicating that there is no charge in the redistribution of the Zr atoms. As shown in Fig. 7(d), the N 1s spectra of PCN-224 can be fitted with two separate peaks, which are attributed to pyrrolic N and pyridinic N. After Mo adsorption,

the peak of pyrrolic N shifted from 398.94 eV to 398.18 eV, suggesting the occurrence of interaction between Mo species and pyrrolic groups, which is consistent with the analysis of FT-IR results. In the C 1s spectra of PCN-224 (see in Fig. S5†), the binding energy of O=C=O moved from 288.2 eV to 288.6 eV and the higher binding energy shift suggests the electron loss of this chemical bond, leading to structural change, which is consistent with the XRD and FT-IR results.

Based on the above analysis, the possible molybdenum adsorption mechanisms seem to be derived by hydrogen bonds, electrostatic attraction and coordination interaction. The following is the summary: (1) The molybdenum species are adsorbed through electrostatic attraction by PCN-222 and PCN-224, when pH < pH_{PZC}; (2) The adsorption sites on the metal clusters (hydroxyl groups) and linkers (pyrrolic N) of PCN-222 serve to interact with molybdenum species through hydrogen bonds, while the interaction between PCN-224 and Mo ions mainly occurred with the linkers; (3) Zr-O-Mo coordination interaction only appears in PCN-222, which is probably ascribed to its higher number of hydroxyl groups (Zr₆(μ₃-OH)₈) and lower volumetric density of TCPP linkers (1.9 mmol cm⁻³) compared with that of PCN-224 (Zr₆(μ₃-O)₄(μ₃-OH)₄ and 3.6 mmol cm⁻³).⁵⁰

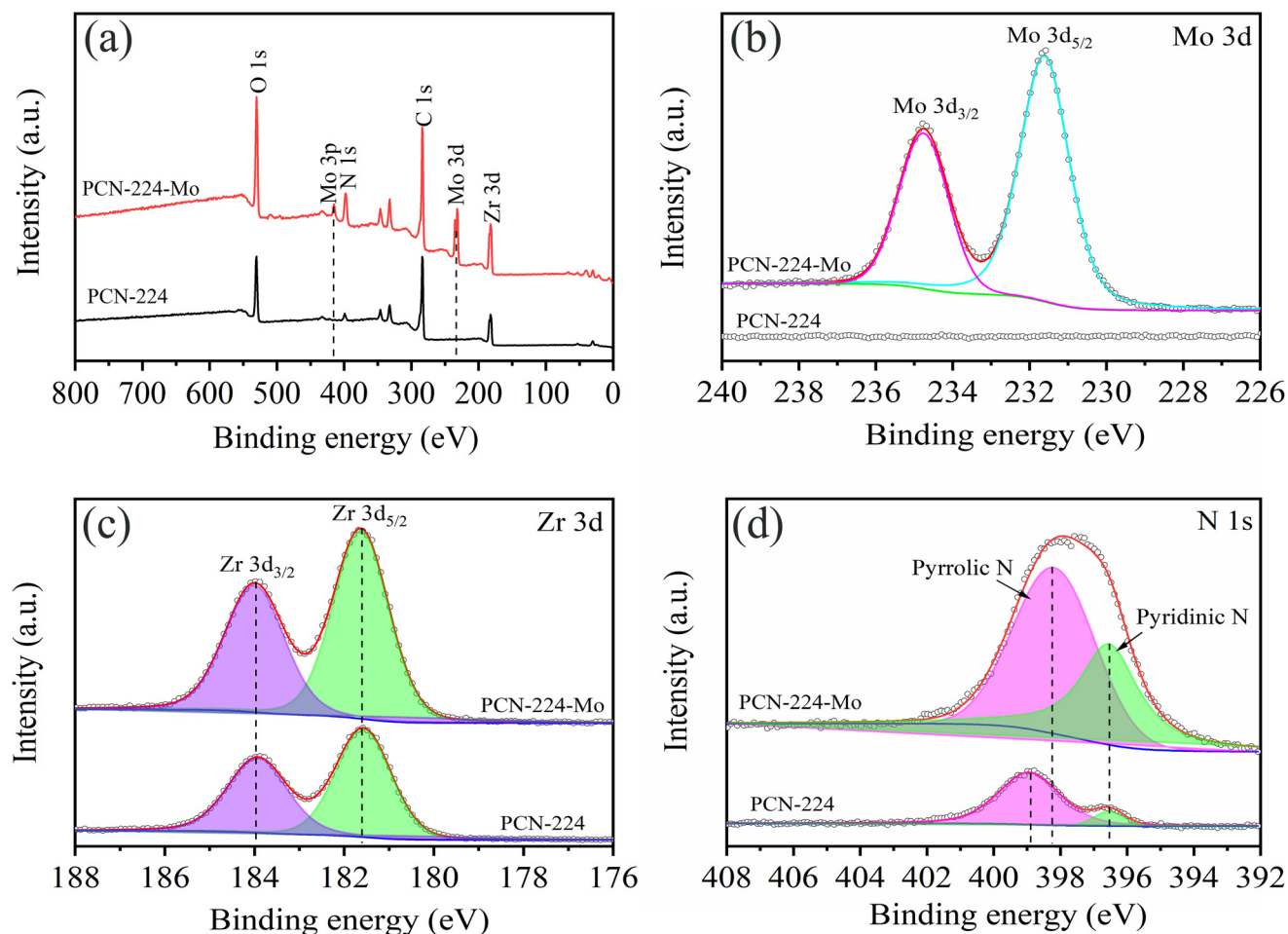


Fig. 7 (a) XPS survey spectra; (b) Mo 3d; (c) Zr 3d and (d) N 1s of PCN-224 before and after molybdenum adsorption.



Table 2 Elution parameters of PCN-222 based $^{99}\text{Mo}/^{99\text{m}}\text{Tc}$ generator using eluent having different pH values

Elution no.	pH	Time of growth (h)	Elution yield (%)	^{99}Mo breakthrough (%)	Zr breakthrough (ppm)
1	6.1	24	31.3	1.9	<0.01
2		24	52.4	2.0	<0.01
3	7.9	25	45.0	2.4	<0.01
4		24	49.0	2.4	<0.01
5	9.6	23	56.4	2.2	<0.01

3.3 PCN-222 and PCN-224 as adsorbents for the $^{99}\text{Mo}/^{99\text{m}}\text{Tc}$ generator

To further support the feasibility of PCN MOFs in practical application, their adsorption performance in batch and column mode was examined utilizing ^{99}Mo . The results showed that the ^{99}Mo batch adsorption capacity of PCN-222 and PCN-224 was 365 mg g^{-1} and 336 mg g^{-1} , respectively, when the initial Mo concentration was 5 mg mL^{-1} , which is consistent with the results obtained using non-active molybdenum. The $^{99\text{m}}\text{Tc}$ elution performance of PCN-222 and PCN-224 as adsorbents for $^{99}\text{Mo}/^{99\text{m}}\text{Tc}$ generator was subsequently evaluated. The generator was washed using saline solution (pH = 6.1) after one day of $^{99\text{m}}\text{Tc}$ ingrowth. The detailed elution results can be found in Tables S5 and S6.† The elution yield of $^{99\text{m}}\text{Tc}$ for PCN-222 and PCN-224 was about 30% and 8%, respectively. The low elution yield was most likely caused by the inappropriate pH (<IEPs) of the saline solution. To improve the elution yield, saline solutions with different pH values were applied to elute the $^{99}\text{Mo}/^{99\text{m}}\text{Tc}$ generator fabricated with PCN-222 as shown in Table 2. It can be observed that the elution efficiency of $^{99\text{m}}\text{Tc}$ increased gradually with the increasing pH of the saline solution, reaching about 56% when the pH of the saline solution was 9.6. Meanwhile, the amount of ^{99}Mo was about 2% in all eluted fractions, which is higher than the limit of 0.1% based on the requirements of the International Pharmacopoeia (IP) (World Health Organization, 2009).⁵¹ The zirconium breakthrough was less than the ICP-OES detection limit (*i.e.* 10 ppb) and is not considered to be a problem. At the same time, the pH of the saline elution had hardly any influence on the $^{99\text{m}}\text{Tc}$ elution efficiency for PCN-224 (Table S7†), showing low efficiencies (~3%), which indicates that PCN-224 could be considered as candidates for the immobilization of technetium. The results show that PCN-222 could be a promising candidate as molybdenum adsorbent for $^{99}\text{Mo}/^{99\text{m}}\text{Tc}$ generator. However, higher elution efficiency and lower molybdenum breakthrough have to be pursued by optimizing the separation conditions for practical medical application in the future.

4. Conclusions

The metal-organic frameworks PCN-222 and PCN-224 were synthesized and their molybdenum adsorption performance was studied at different pH and molybdenum concentrations. The molybdenum adsorption capacity of PCN-222 and PCN-224 could reach up to 525 mg g^{-1} and 455 mg g^{-1} ,

respectively. XPS, FT-IR and zeta potential were employed to understand the interaction between molybdenum ions and MOFs. It was demonstrated that high surface area MOFs with big porous structures can improve molybdenum adsorption capacity by electrostatic attraction, hydrogen bond and coordination bonds. The $^{99\text{m}}\text{Tc}$ elution yield of $^{99}\text{Mo}/^{99\text{m}}\text{Tc}$ generator using PCN-222 and PCN-224 as adsorbents was about 30% and 8%, respectively, when the pH of the saline solution was 6.1. A higher elution yield (56%) for the PCN-222 based generator can be obtained by increasing the pH of the saline solution to 9.6, but a relatively high ^{99}Mo breakthrough (~2%) was observed. Future studies will be done by improving $^{99\text{m}}\text{Tc}$ elution yield and reducing ^{99}Mo breakthrough under different conditions so that PCN-222 possessing high molybdenum adsorption capacity can be used as adsorbent for the $^{99}\text{Mo}/^{99\text{m}}\text{Tc}$ generator in eventual clinical application.

Author contributions

Chao Ma: conceptualization; data curation; formal analysis; methodology; validation; writing—original draft. Hubert T. Wolterbeek: supervision. Antonia G. Denkova: supervision; funding acquisition; project administration; writing—review & editing. Pablo Serra Crespo: supervision; funding acquisition; conceptualization; project administration; methodology; writing—review & editing.

Conflicts of interest

The authors declare that they have no known competing financial interests or personal relationships that could have appeared to influence the work reported in this paper.

Acknowledgements

The authors are thankful to the China Scholarship Council (Grant No. 201807040061). The authors are grateful to Willy Rook for her help with the N_2 adsorption measurements. We gratefully acknowledge Bart Boshuizen for the XPS measurement. The authors are grateful to Andrea Garcia-Junceda Ameigenda for the SEM pictures. The authors appreciate Katalin Gmeling in the Institute for Energy Security and Environmental Safety Centre for Energy Research, Hungary for the supply of ^{99}Mo .



References

- 1 M. Pillai, A. Dash and F. R. Knapp, Radionuclide generators: a ready source diagnostic and therapeutic radionuclides for nuclear medicine applications, *Radiopharmaceuticals: application, insights and future*, 2016, pp. 63–118.
- 2 W. C. Eckelman, Unparalleled contribution of ^{99m}Tc to medicine over 5 decades, *JACC Cardiovasc Imaging*, 2009, **2**, 364–368.
- 3 S. Hasan and M. A. Prelas, Molybdenum-99 production pathways and the sorbents for $^{99}\text{Mo}/^{99m}\text{Tc}$ generator systems using (n, γ) ^{99}Mo : a review, *SN Appl. Sci.*, 2020, **2**, 1–28.
- 4 M. R. Pillai, A. Dash and F. F. Knapp, Sustained availability of ^{99m}Tc : possible paths forward, *J. Nucl. Med.*, 2013, **54**, 313–323.
- 5 R. Van Noorden, Radioisotopes: The medical testing crisis, *Nature*, 2013, **504**, 202–204.
- 6 T. Takeda, M. Fujiwara, M. Kurosawa, N. Takahashi, M. Tamura, T. Kawabata, Y. Fujikawa, K. N. Suzuki, N. Abe, T. Kubota and T. Takahashi, ^{99m}Tc production via the (γ , n) reaction on natural Mo, *J. Radioanal. Nucl. Chem.*, 2018, **318**, 811–821.
- 7 J. Stillman, E. Feldman, S. Pham, D. Yoon, E. Wilson, W. Cowherd, L. Foyto, K. Kutikkad and N. Peters, *Safety Analysis of the Mo-99 Production Upgrade to the University of Missouri Research Reactor (MURR) with Highly-Enriched and Low-Enriched Uranium Fuel*, Argonne National Lab.(ANL), Argonne, IL (United States), 2019.
- 8 M. R. Pillai and F. F. Knapp, Molybdenum-99 production from reactor irradiation of molybdenum targets: a viable strategy for enhanced availability of technetium-99 m, *Q. J. Nucl. Med. Mol. Imaging*, 2012, **56**, 385–399.
- 9 M. Mostafa, M. Atef and M. A. El-Amir, Preparation and performance studies of $^{99}\text{Mo}/^{99m}\text{Tc}$ column generators based on nano zirconium molybdate, *J. Radioanal. Nucl. Chem.*, 2017, **314**, 1683–1694.
- 10 H. Arino and H. H. Kramer, Fission product ^{99m}Tc generator, *Int. J. Appl. Radiat. Isot.*, 1975, **26**, 301–303.
- 11 R. Chakravarty, R. Ram, R. Mishra, D. Sen, S. Mazumder, M. R. A. Pillai and A. Dash, Mesoporous Alumina (MA) based double column approach for development of a clinical scale $^{99}\text{Mo}/^{99m}\text{Tc}$ generator using (n, γ) ^{99}Mo : an enticing application of nanomaterial, *Ind. Eng. Chem. Res.*, 2013, **52**, 11673–11684.
- 12 A. G. Denkova, B. E. Terpstra, O. M. Steinbach, J. T. Dam and H. T. Wolterbeek, Adsorption of molybdenum on mesoporous aluminum oxides for potential application in nuclear medicine, *Sep. Sci. Technol.*, 2013, **48**, 1331–1338.
- 13 Q. M. Qazi and M. Ahmad, Preparation and evaluation of hydrous titanium oxide as a high affinity adsorbent for molybdenum (^{99}Mo) and its potential for use in ^{99m}Tc generators, *Radiochim. Acta*, 2011, **99**, 231.
- 14 R. Chakravarty, R. Shukla, R. Ram, A. K. Tyagi, A. Dash and M. Venkatesh, Practicality of tetragonal nano-zirconia as a prospective sorbent in the preparation of $^{99}\text{Mo}/^{99m}\text{Tc}$ generator for biomedical applications, *Chromatographia*, 2010, **72**, 875–884.
- 15 R. Chakravarty, R. Shukla, S. Gandhi, R. Ram, A. Dash, M. Venkatesh and A. K. Tyagi, Polymer embedded nanocrystalline titania sorbent for $^{99}\text{Mo}/^{99m}\text{Tc}$ generator, *J. Nanosci. Nanotechnol.*, 2008, **8**, 4447–4452.
- 16 R. Chakravarty, R. Shukla, R. Ram, M. Venkatesh, A. Dash and A. K. Tyagi, Nanoceria-PAN composite-based advanced sorbent material: a major step forward in the field of clinical-grade $^{68}\text{Ge}/^{68}\text{Ga}$ generator, *ACS Appl. Mater. Interfaces*, 2010, **2**, 2069–2075.
- 17 W. G. Cui, T. L. Hu and X. H. Bu, Metal–Organic Framework Materials for the Separation and Purification of Light Hydrocarbons, *Adv. Mater.*, 2020, **32**, 1806445.
- 18 B. M. Jun, Y. A. Al-Hamadani, A. Son, C. M. Park, M. Jang, A. Jang, N. C. Kim and Y. Yoon, Applications of metal-organic framework-based membranes in water purification: A review, *Sep. Purif. Technol.*, 2020, **247**, 116947.
- 19 M. X. Wu and Y. W. Yang, Metal-Organic Framework (MOF)-Based Drug/Cargo Delivery and Cancer Therapy, *Adv. Mater.*, 2017, **29**, 1606134.
- 20 G. R. Xu, Z. H. An, K. Xu, Q. Liu, R. Das and H. L. Zhao, Metal organic framework (MOF)-based micro/nanoscaled materials for heavy metal ions removal: The cutting-edge study on designs, synthesis, and applications, *Coord. Chem. Rev.*, 2021, **427**, 213554.
- 21 S. W. Lv, J. M. Liu, C. Y. Li, N. Zhao, Z. H. Wang and S. Wang, A novel and universal metal-organic frameworks sensing platform for selective detection and efficient removal of heavy metal ions, *Chem. Eng. J.*, 2019, **375**, 122111.
- 22 J. Li, X. Wang, G. Zhao, C. Chen, Z. Chai, A. Alsaedi, T. Hayat and X. Wang, Metal-organic framework-based materials: superior adsorbents for the capture of toxic and radioactive metal ions, *Chem. Soc. Rev.*, 2018, **47**, 2322–2356.
- 23 S. Rojas and P. Horcajada, Metal-Organic Frameworks for the Removal of Emerging Organic Contaminants in Water, *Chem. Rev.*, 2020, **120**, 8378–8415.
- 24 C. Ma, A. Vasileiadis, H. T. Wolterbeek, A. G. Denkova and P. Serra Crespo, Adsorption of molybdenum on Zr-based MOFs for potential application in the $^{99}\text{Mo}/^{99m}\text{Tc}$ generator, *Appl. Surf. Sci.*, 2022, **572**, 151340.
- 25 C. Ma, H. T. Wolterbeek, A. G. Denkova and P. Serra Crespo, A cerium-based metal-organic framework as adsorbent for the $^{99}\text{Mo}/^{99m}\text{Tc}$ generator, *Sep. Purif. Technol.*, 2022, **295**, 121218.
- 26 W. Morris, B. Voloskiy, S. Demir, F. Gandara, P. L. McGrier, H. Furukawa, D. Cascio, J. F. Stoddart and O. M. Yaghi, Synthesis, structure, and metalation of two new highly porous zirconium metal-organic frameworks, *Inorg. Chem.*, 2012, **51**, 6443–6445.
- 27 J. Hynek, S. Ondrusova, D. Buzek, P. Kovar, J. Rathousky and J. Demel, Postsynthetic modification of a zirconium metal-organic framework at the inorganic secondary build-



- ing unit with diphenylphosphinic acid for increased photo-sensitizing properties and stability, *Chem. Commun.*, 2017, **53**, 8557–8560.
- 28 J. Park, Q. Jiang, D. Feng, L. Mao and H. C. Zhou, Size-Controlled Synthesis of Porphyrinic Metal-Organic Framework and Functionalization for Targeted Photodynamic Therapy, *J. Am. Chem. Soc.*, 2016, **138**, 3518–3525.
 - 29 M. Lee, S. Sohn and M. Lee, Ionic Equilibria and Ion Exchange of Molybdenum(VI) from Strong Acid Solution, *Bull. Korean Chem. Soc.*, 2011, **32**, 3687–3691.
 - 30 J. Morales-Santelices, M. Colet-Lagrange and M. García-García, Speciation model of the Mo(VI)-Ni(II)-Citrate-S(VI)-N(III) aqueous system for the study of the electrodeposition of molybdenum and nickel oxides films, *J. Electrochem. Soc.*, 2018, **165**, 344–353.
 - 31 X. Liu, J. Sun, X. Xu, A. Alsaedi, T. Hayat and J. Li, Adsorption and desorption of U(VI) on different-size graphene oxide, *Chem. Eng. J.*, 2019, **360**, 941–950.
 - 32 T. Guo, Y. Lei, X. Hu, G. Yang, J. Liang, Q. Huang, X. Li, M. Liu, X. Zhang and Y. Wei, Hydrothermal synthesis of MXene-MoS₂ composites for highly efficient removal of pesticides, *Appl. Surf. Sci.*, 2022, **588**, 152597.
 - 33 J. Serrano Gómez and F. Granados Correa, ^{99m}Tc generator with hydrated MnO₂ as adsorbent of ⁹⁹Mo, *J. Radioanal. Nucl. Chem.*, 2002, **254**, 625–628.
 - 34 Y. Suzuki, T. Kitagawa, Y. Namekawa, M. Matsukura, K. Nishikata, H. Mimura and K. Tsuchiya, Molybdenum Adsorption and Desorption Properties of Alumina with Different Surface Structures for ⁹⁹Mo/^{99m}Tc Generators, *Trans. Mater. Res. Soc. Jpn.*, 2018, **43**, 75–80.
 - 35 I. Saptiama, Y. V. Kaneti, Y. Suzuki, K. Tsuchiya, N. Fukumitsu, T. Sakae, J. Kim, Y. M. Kang, K. Ariga and Y. Yamauchi, Template-Free Fabrication of Mesoporous Alumina Nanospheres Using Post-Synthesis Water-Ethanol Treatment of Monodispersed Aluminium Glycerate Nanospheres for Molybdenum Adsorption, *Small*, 2018, **14**, 1800474.
 - 36 R. Chakravarty, R. Ram, A. Dash and M. R. Pillai, Preparation of clinical-scale ⁹⁹Mo/^{99m}Tc column generator using neutron activated low specific activity ⁹⁹Mo and nanocrystalline γ -Al₂O₃ as column matrix, *Nucl. Med. Biol.*, 2012, **39**, 916–922.
 - 37 H. E. Ramadan, M. A. El-Amir and M. Mostafa, Adsorption studies of molybdate(VI)-(99)Mo onto nano zirconium hydroxide gel, *Appl. Radiat. Isot.*, 2022, **181**, 110092.
 - 38 J. Wang, R. Gao, Q. Huang, X. Yin, M. Lin, S. Cao, D. Chen, F. Fan, X. Wu, Z. Qin, Z. Guo, J. Bai, J. Chu, W. Tian, C. Tan, B. Li, N. Cheng and Z. Jia, Practicality of hierarchically macro/mesoporous gamma-Al₂O₃ as a promising sorbent in the preparation of low specific activity ⁹⁹Mo/^{99m}Tc generator, *Appl. Radiat. Isot.*, 2021, **178**, 109986.
 - 39 M. Amin, M. A. El-Amir, H. E. Ramadan and H. El-Said, ⁹⁹Mo/^{99m}Tc generators based on aluminum molybdate gel matrix prepared by nano method, *J. Radioanal. Nucl. Chem.*, 2018, **318**, 915–922.
 - 40 D. Feng, W. C. Chung, Z. Wei, Z. Y. Gu, H. L. Jiang, Y. P. Chen, D. J. Darensbourg and H. C. Zhou, Construction of ultrastable porphyrin Zr metal-organic frameworks through linker elimination, *J. Am. Chem. Soc.*, 2013, **135**, 17105–17110.
 - 41 D. Feng, Z. Y. Gu, J. R. Li, H. L. Jiang, Z. Wei and H. C. Zhou, Zirconium-metalloporphyrin PCN-222: mesoporous metal-organic frameworks with ultrahigh stability as biomimetic catalysts, *Angew. Chem., Int. Ed.*, 2012, **51**, 10307–10310.
 - 42 X. Zhu, B. Li, J. Yang, Y. Li, W. Zhao, J. Shi and J. Gu, Effective adsorption and enhanced removal of organophosphorus pesticides from aqueous solution by Zr-based MOFs of UiO-67, *ACS Appl. Mater. Interfaces*, 2015, **7**, 223–231.
 - 43 Y. Zhan, Y. Liu, H. Zu, Y. Guo, S. Wu, H. Yang, Z. Liu, B. Lei, J. Zhuang, X. Zhang, D. Huang and C. Hu, Phase-controlled synthesis of molybdenum oxide nanoparticles for surface enhanced Raman scattering and photothermal therapy, *Nanoscale*, 2018, **10**, 5997–6004.
 - 44 W. Zhu, X. Huang, Y. Zhang, Z. Yin, Z. Yang and W. Yang, Renewable molybdate complexes encapsulated in anion exchange resin for selective and durable removal of phosphate, *Chin. Chem. Lett.*, 2021, **32**, 3382–3386.
 - 45 N. Wang, S. Y. Liu, Z. Q. Sun, Y. D. Han, J. L. Xu, Y. Xu, J. B. Wu, H. Meng, B. S. Zhang and X. Zhang, Synergistic adsorption and photocatalytic degradation of persist synthetic dyes by capsule-like porphyrin-based MOFs, *Nanotechnology*, 2021, **32**, 465705.
 - 46 L. Wang, P. X. Jin, S. H. Duan, J. W. Huang, H. D. She, Q. Z. Wang and T. C. An, Accelerated Fenton-like kinetics by visible-light-driven catalysis over iron(III) porphyrin functionalized zirconium MOF: effective promotion on the degradation of organic contaminants, *Environ. Sci. Nano*, 2019, **6**, 2652–2661.
 - 47 H. Jia, D. Ma, S. Zhong, L. Li, L. Li, L. Xu and B. Li, Boosting photocatalytic activity under visible-light by creation of PCN-222/g-C₃N₄ heterojunctions, *Chem. Eng. J.*, 2019, **368**, 165–174.
 - 48 G. Q. Lv, S. W. Chen, H. F. Zhu, M. Li and Y. X. Yang, Pyridinic-nitrogen-dominated nitrogen-doped graphene stabilized Cu for efficient selective oxidation of 5-hydroxymethylfurfural, *Appl. Surf. Sci.*, 2018, **458**, 24–31.
 - 49 Q. Q. Zhu, W. W. Zhang, H. W. Zhang, R. R. Yuan and H. M. He, Elaborately manufacturing an electrochemical aptasensor based on gold nanoparticle/COF composites for amplified detection performance, *J. Mater. Chem. C*, 2020, **8**, 16984–16991.
 - 50 X. Gong, Y. Shu, Z. Jiang, L. Lu, X. Xu, C. Wang and H. Deng, Metal-Organic Frameworks for the Exploitation of Distance between Active Sites in Efficient Photocatalysis, *Angew. Chem., Int. Ed.*, 2020, **59**, 5326–5331.
 - 51 Sodium Pertechnetate (^{99m}Tc) Injection (Non-fission): Revised Final text for addition to The International Pharmacopoeia, World Health Organization, 2009.

